1. SCIENTIFIC RESEARCH

CONDENSED MATTER PHYSICS

The main objectives of research in the framework of the theme involved the application of neutron scattering techniques and complementary methods to investigate the structure, dynamics and microscopic properties of nanosystems and novel materials, which are of great importance for the development of nanotechnologies in the fields of electronics, pharmacology, medicine, chemistry, modern condensed matter physics and interdisciplinary sciences.

In 2015, the greater part of experimental research was carried out on the spectrometers of the modernized IBR-2 reactor in accordance with the Topical Plan for JINR Research and International Cooperation and FLNP User Program. A number of scientific experiments were performed in neutron and synchrotron centers in Russia and abroad under the existing cooperation agreements and accepted beam time application proposals. Also, the activities on the modernization of the available spectrometers and the development of new instruments were carried out in accordance with the development program plan for the IBR-2 spectrometers. Most attention was given to the realization of the top-priority projects (creation of the final configuration of a new DN-6 diffractometer for studying microsamples and a multipurpose GRAINS reflectometer).

Within the framework of investigations under the theme the employees of the FLNP Department of Neutron Investigations of Condensed Matter (NICM) maintained broad cooperation with many scientific organizations in Russia and abroad. The cooperation, as a rule, was documented by joint protocols or agreements. In Russia, especially active collaboration was with the thematically-close organizations, such as RRC KI, PNPI, SSC RF IPPE, MSU, IMP UB RAS, IC RAS, INR RAS and others.

A list of the main scientific topics studied by the employees of the NICM Department includes:

- Investigation of the structure and properties of novel functional materials;
- Investigation of the structure and properties of materials under extreme conditions;
- Investigation of fundamental regularities of real-time processes in condensed matter;
- Investigation of atomic dynamics of materials for nuclear power engineering;
- Computer simulation of physical and chemical properties of novel crystalline and nanostructured materials;
- Investigation of magnetic properties of layered nanostructures;
- Investigation of structural characteristics of carbon- and silicon-containing nanomaterials;
- Investigation of molecular dynamics of nanomaterials;
- Investigation of magnetic colloidal systems in bulk and at interfaces;
- Structural analysis of polymer nanodispersed materials;
- Investigation of supramolecular structure and functional characteristics of biological materials;
- Investigation of structure and properties of lipid membranes and lipid complexes;
- Investigation of texture and physical properties of Earth's rocks, minerals and engineering materials;
- Non-destructive control of internal stresses in industrial products and engineering materials;
- Introscopy of internal structure and processes in industrial products, rocks and natural heritage objects.

1. Scientific results

1.1. Structure investigations of novel oxide, intermetallic and nanostructured materials

The magnetic, structural, and vibrational properties of YMn_2O_5 multiferroic with a strong magnetoelectric coupling have been studied by means of neutron, x-ray diffraction, and Raman spectroscopy at pressures up to 30 GPa in a temperature range from 10 to 300 K [1] (**Fig. 1**). The application of high pressure (P > 1 GPa) resulted in a suppression of commensurate and incommensurate antiferromagnetic (AFM) phases with a propagation vector $q = (\sim1/2, 0, \sim1/4)$ and appearance of a new commensurate AFM phase with $q_p = (1/2, 0, 1/2)$. This observation is in sharp contrast to a general trend towards the stabilization of the commensurate AFM phase with the propagation vector q = (1/2, 0, 1/4) found in other RMn_2O_5 compounds under pressure. At higher pressures P > 16 GPa a structural phase transition accompanied by anomalies in the pressure behavior of some unit cell parameters and vibrational modes was observed. The obtained data allowed us to analyze the role of competing magnetic interactions in the formation of the magnetic ground state of RMn_2O_5 multiferroics.

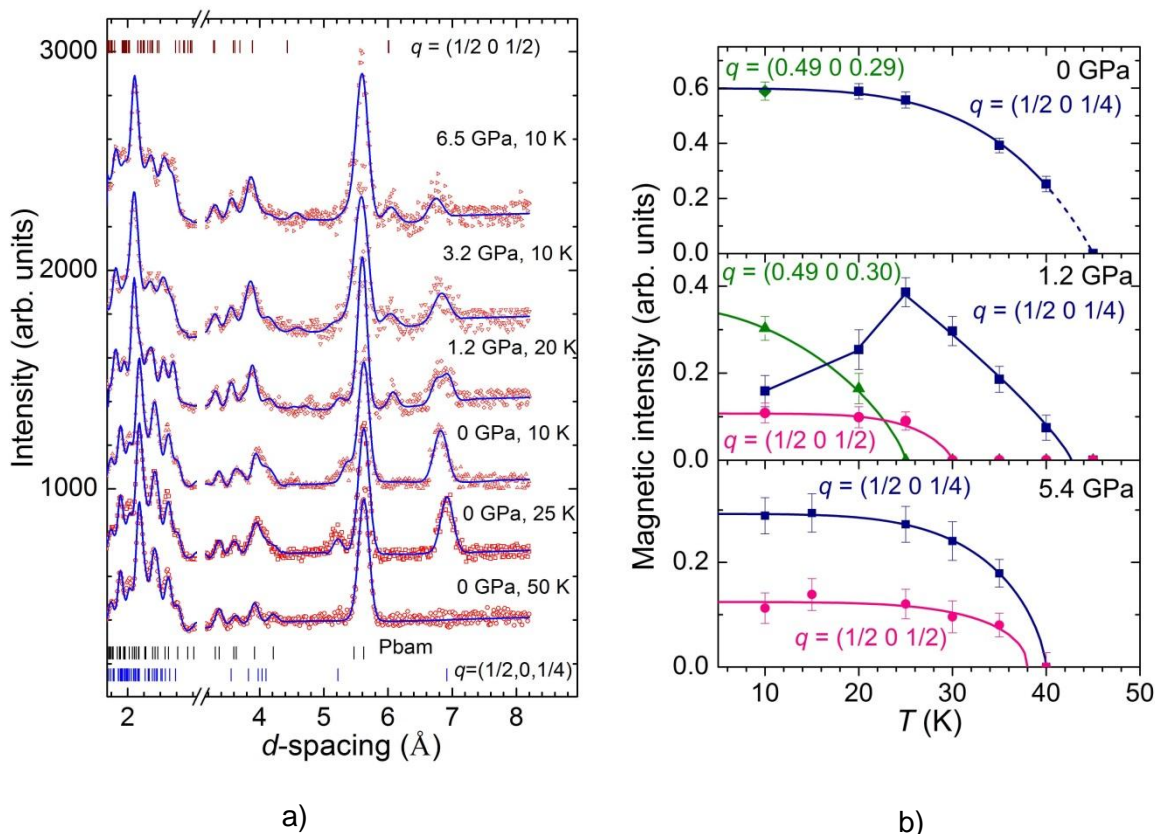a)   b)

Fig. 1. Neutron diffraction spectra of YMn_2O_5 obtained at different pressures and temperatures with the DN-12 diffractometer and treated with the Rietveld method (a). Temperature dependences of integrated intensity of peaks $(1-q_x, -1, -q_z)/(1-q_x, 1, -q_z)/(\pm q_x, 1, \pm q_z)$ of commensurate and incommensurate AFM phases with a propagation vector $q = (\sim1/2, 0, \sim1/4)$ and a peak $(-q_x, 1, 1-q_z)$ of commensurate AFM phase with a propagation vector $q_p = (1/2\ 0\ 1/2)$ under various pressures (b).

1. SCIENTIFIC RESEARCH

The structural characteristics of promising high-voltage cathode materials on the basis of $LiNi_{0.5}Mn_{1.5}O_4$ - $LiNi_{0.5-x}Mn_{1.5-y}M_{x+y}O_4$ (M=Co, Cr, Ti, Al, Mg; x+y=0.05) synthesized in the Institute of Solid State Chemistry and Mechanochemistry, SB RAS (Novosibirsk) have been studied in order to improve their electrochemical properties [2]. Unsubstituted $LiNi_{0.5}Mn_{1.5}O_4$ is characterized by a high potential (4.7 V) corresponding to a flat plateau in a charge-discharge characteristic at an average capacity of 120 mAh/g, which significantly increases the specific stored energy of the battery compared to other materials ($LiCoO_2$ ~3.8 V, $LiFePO_4$ ~3.2 V at the same capacity). Depending on the method of synthesis $LiNi_{0.5}Mn_{1.5}O_4$ may have either a primitive cubic $P4_332$ symmetry with an ordered arrangement of cations (in this case the synthesis temperature should not exceed 700°C) or a face-centered cubic Fd-3m symmetry and disordered arrangement of cations (formed at temperatures above 800°C). Due to the structural transformations during cycling the $LiNi_{0.5}Mn_{1.5}O_4$ compound with a $P4_332$ space group shows poorer electrochemical behavior than $LiNi_{0.5}Mn_{1.5}O_4$ with a Fd-3m structure. Samples for the study were synthesized at T < 800°C by means of a small substitution of other transition metals for Ni and Mn cations and mechanical activation of the reagent mixture in a planetary mill. As a result of the treatment of the neutron diffraction spectra using the Rietveld method it has been revealed that all the samples under study have a two-phase structure, with a phase having an Fd-3m space group being a dominant one and a secondary phase with a $P4_332$ space group ranging from 1 to 20% depending on the substitution metal and the synthesis temperature. It has been found that the dopants preferably substitute for Ni ions, which in turn results in the appearance of a NiO impurity phase in a small amount (1-2%). The average crystal size was 70-80 nm for the samples synthesized at 700°C, and 100-150 nm for the samples synthesized at 800°C. As expected, large microstrains were found to be more frequent in the samples with lower synthesis temperature.

A study of the evolution of the crystalline structure of the cathode material $LiNi_{0.8}Co_{0.1}Al_{0.1}O_2$ in the process of electrochemical cycling has been carried out using neutron diffraction (**Fig. 2**). The experiments were performed on the RTD (Real-Time-Diffractometer) diffractometer. Compositions of $LiNi_xCo_yAl_{1-x-y}O_2$ type are just starting to be introduced in mass production of lithium-ion batteries as a positive electrode (cathode), gradually replacing the widespread lithium cobaltate. Earlier such compounds were studied in real time during electrochemical cycling only in model cells by x-ray diffraction. Neutron diffraction makes it possible to study structural changes in the electrode materials both in specialized electrochemical cells and immediately in finished products. This study investigated a Li-Ion 18650 cylindrical rechargeable battery, where graphite is used as a negative electrode and $LiNi_xCo_yAl_{1-x-y}O_2$ with $x \approx 0.8$ and $y \approx 0.1$ (the values were specified during the treatment of the obtained diffraction data) as a positive electrode. The crystal structure of $LiNi_xCo_yAl_{1-x-y}O_2$ in a completely discharged battery corresponds to a space group R-3m with unit cell parameters a = 2.8453(1) and c = 14.1878(2) Å. On the basis of the analysis of experimental data obtained in the course of several charge-discharge cycles performed at different rates (C/3 and C/10, where C is the full capacity) it has been shown that the intercalation of lithium into graphite proceeds with the successive formation of several LiC_n phases. The formation of final LiC_6 phase during charging is easily detected by a step-like appearance of a diffraction peak at $d \approx 3.67$ Å. The phase separation in the cathode material $LiNi_{0.8}Co_{0.1}Al_{0.1}O_2$, which can be observed, for example, in $LiNi_{0.8}Co_{0.15}Al_{0.05}O_2$, has not been found. At the same time, the unit cell parameters of the two materials change during charging in a similar manner, and the expansion and subsequent contraction of the unit cell proceed anisotropically. When charging, at first the cell expands along the hexagonal c axis and slightly contracts in the basal plane (a and b axes). Towards the end of charging, there occur an abrupt contraction along the c axis and some expansion along the a and b axes.
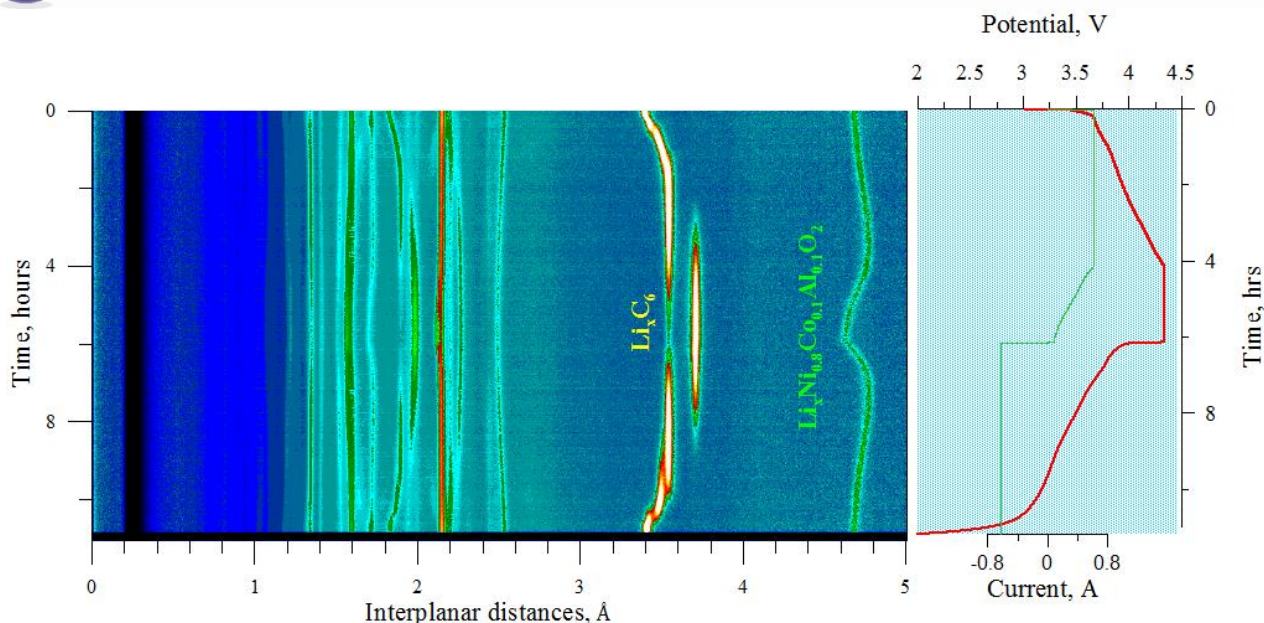
Fig. 2. The evolution of neutron diffraction spectra obtained in the real-time (operando) study of LiNi$_{0.8}$Co$_{0.1}$Al$_{0.1}$O$_2$ cathode material using high-intensity neutron diffraction. At the right: charge-discharge curve of the power source during the experiment.

Methods for obtaining different compounds in the nanostructured state have been developing in recent years. The VC$_{0.875}$ compound was the first carbide in whose coarse-grained powder a nanostructure was created as a result of the disorder-order transformation (VC$_{0.875}$ → V$_8$C$_7$). The atomic-vacancy ordering makes it possible to create the nanostructure in the VC$_{0.875}$ bulk carbide. However, until recently it was unclear whether the superstructure V$_8$C$_7$ remains after milling the ordered vanadium carbide to a nanopowder with the average particle size of 400-500 Å and less.

The crystal structure and microstructure of coarse- and nanocrystalline disperse ordered carbide V$_8$C$_7$, which was prepared by milling the initial coarse-crystalline powder for 10 h in a planetary ball mill, were studied with the HRFD diffractometer [3,4]. According to the scanning electron microscopy data, the initial powder ~V$_8$C$_7$ consists of large particles with a size of 3–5 μm, the microstructure of which is a set of curved lobes with diameters from 400 to 600 nm and thicknesses of about 15–20 nm. The nanopowder V$_8$C$_7$ obtained by milling for 10 h consists of nanoparticles with sizes of 20–60 nm united in friable agglomerates with the size from ~400 nm to ~1 μm.

All obtained spectra of the coarse-grained powder ~V$_8$C$_7$ include weak superstructure reflections of the ordered phase V$_8$C$_7$. For the coarse-grained vanadium carbide ~VC$_{0.875}$ (V$_8$C$_7$), the dependence of the width of diffraction peaks on the interplanar distances, $\Delta d^2(d^2)$, is linear, indicating that there is no size effect. For the nanopowder the diffraction peaks are strongly broadened and the dependence $\Delta d^2(d^2)$ is parabolic, from which it follows that the average size of the nanopowder particles is about 190 Å. Also, the presence of the disordered phase VC$_{0.875}$ with the structure B1, the lattice period of which is $a_{B1} < a_{V_8C_7}/2$, was found in the samples under study. The analysis revealed that the disordered phase represents small-size inclusions (~500 Å) in the matrix of the ordered phase V$_8$C$_7$, and its content in the coarse-crystalline powder is (21 ± 3) wt %. The real structure of the ordered phase is characterized by a lowered content of carbon as compared to the ideal one, which corresponds to the chemical composition V$_8$C$_{7-\delta}$, where $\delta \cong 0.03$.

1. SCIENTIFIC RESEARCH

The vanadium carbide nanopowder also contains the ordered and disordered phases (**Fig. 3**), but as a result of milling, the amount of the latter is (45 ± 10) wt %. The periods of cubic unit cells of phases V_8C_7 and $VC_{0.875}$ in the nanopowder are slightly smaller than in the coarse-crystalline powder.
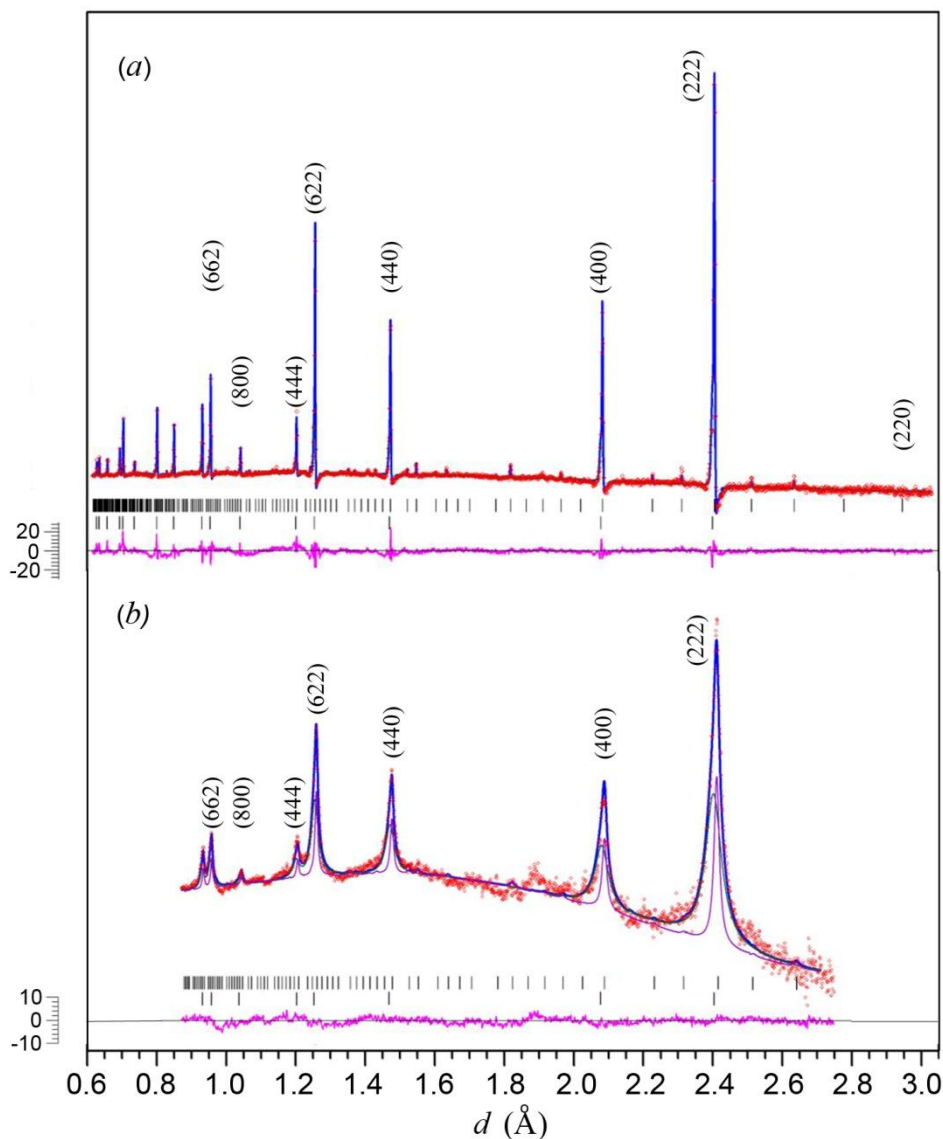

Fig. 3. Refinement of the neutron diffraction patterns of vanadium carbide powders (measurements in a high-resolution mode by detectors placed at the scattering angle 2θ = 152°): (a) initial coarse-grained powder and (b) nanopowder. The disordered phase is present in the samples along with the main ordered phase. Contributions of the ordered (narrow peaks) and disordered (wide peaks) are shown for the nanopowder. Vertical marks in the upper and lower rows indicate the positions of reflections of the ordered phase $V_8C_{7-\delta}$ ($\delta \cong 0.03$) and the disordered phase $VC_{0.875}$, respectively.

Taking into account the limitations on the accuracy of determination of the filling of positions of C atoms it is believed that the nanocrystalline ordered phase has the same composition $V_8C_{7-\delta}$, $\delta \cong 0.0$ as that in the coarse-grained powder. The displacements of carbon atoms C3 and C4 in the lattice of the nanocrystalline ordered phase $V_8C_{7-\delta}$ are small. At the same time, the displacements of the same

atoms are larger in the coarse-grained ordered phase. This is due to the noticeable deformation distortions of the lattice during milling of the powder.

The structural investigation of a solid solution of $BaFe_{12-x}Al_xO_{19}$ barium ferrites with a partial replacement of iron by diamagnetic aluminum ions (x = 0.1 - 1.2) has been performed using the neutron diffraction method [5]. In the entire investigated range of aluminum concentrations barium hexaferrite retains the structure of magnetoplumbite, and its magnetic structure can be described by the Gorter's model with the orientation of moments along the hexagonal axis. The total magnetic moment per formula unit decreases with the replacement of iron ions with diamagnetic aluminum ions. The increase in the unit cell volume with increasing x can be explained by the larger ionic radius of Al ions replacing Fe ions. At low temperatures (10 – 150 K) the Invar effect has been observed, i.e. the coefficient of thermal expansion is practically zero. With growing concentration of Al ions an increase of microstrains in crystallites has been found, which is connected with the different ionic radii of Fe and Al ions.

The crystal and magnetic structure of nanostructured manganites $La_{1-x}Sr_xMnO_3$ (x = 0.28, 0.37) has been studied in the pressure range of 0 - 4.5 GPa and temperature range of 5 - 300 K [6]. The physical properties of these compounds in the nanostructured state differ significantly from those in the bulk holding much promise for applications in biomedical technologies. In both compounds the ferromagnetic ordering is formed at temperatures close to room temperature, and at low temperatures (T < 270 K) the appearance of an additional A-type AFM phase is observed (**Fig. 4**). At higher pressures the volume fraction of AFM phase increases and that of FM phase decreases. The obtained results were interpreted in the framework of the "core-shell" model of the formation of nanoparticles in which the core is ferromagnetic and the shell is antiferromagnetic. The observed behavior of the volume of magnetic phases points to an increase in the thickness of the shell of nanoparticles under pressure.
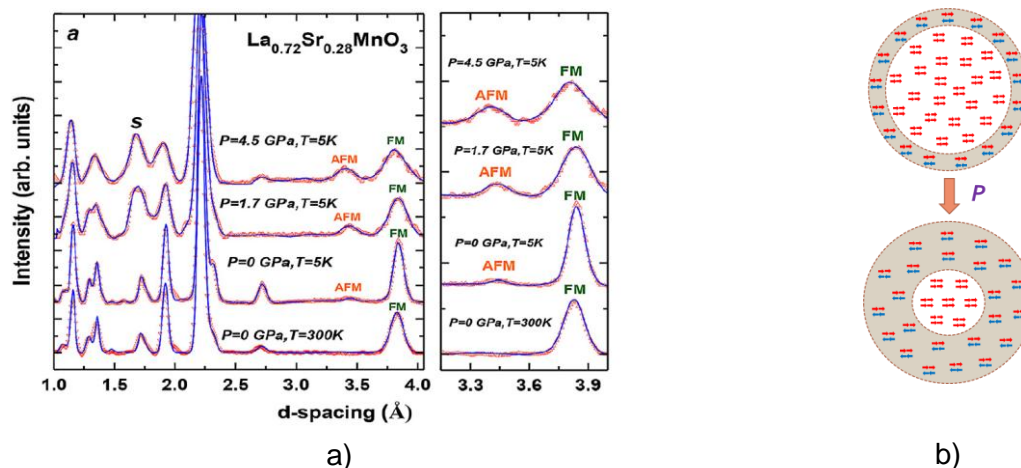

a)   b)

Fig. 4. Neutron diffraction spectra of nanostructured manganite La$_{0.72}$Sr$_{0.28}$MnO$_3$ obtained at different pressures and temperatures with the DN-12 diffractometer and treated using the Rietveld method (a). "Core-shell" model of nanoparticles and their structural evolution under pressure (b).

1.2. Investigations of magnetic fluids and nanoparticles

In the framework of the study of the adsorption of magnetic nanoparticles on solid surfaces the experiments on neutron reflectometry with a horizontal sample plane were continued for the interface of magnetic fluids with crystalline silicon using different treatment of the surface of a solid support.

1. SCIENTIFIC RESEARCH

Thus, when contacting a solid hydrophilic surface, aqueous magnetic fluids characterized by the presence of a number of stable aggregates in solution form a single adsorption layer of non-aggregated nanoparticles at the interface [7]. Moreover, in the experiments with different configurations ('crystal on top' or 'crystal at bottom') a substantial difference in the critical angle of total reflection is observed pointing in the second case to an increase in the concentration of nanoparticles of the magnetic fluid at the interface due to the gravitational effect (**Fig. 5**). One can conclude that in contrast to magnetic fluids on weakly polar solvents, where the adsorption mechanism is mainly determined by gravitational sedimentation, in the aqueous magnetic fluids adsorption occurs mainly due to the electrostatic interaction between the nanoparticles with the substrate surface. The study has been carried out in collaboration with the Institute of Experimental Physics, Slovak Academy of Sciences (Kosice, Slovakia), Faculty of Physics of the Taras Shevchenko National University of Kiev (Kiev, Ukraine), research Institutes of the Romanian Academy of Sciences (Bucharest-Timisoara, Romania) and the Max Planck Institute for Solid State Physics (Stuttgart, Germany).

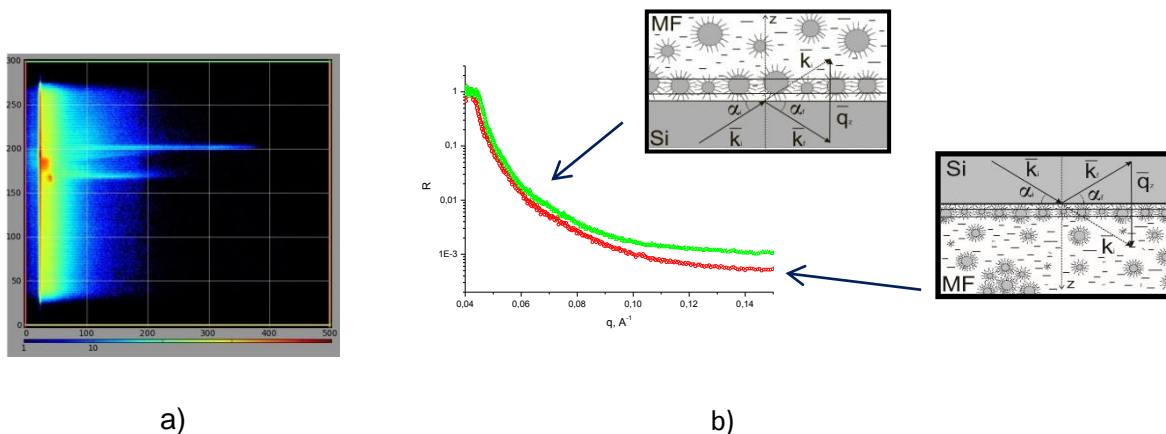a)   b)

Fig. 5. (a) 1D spectrum (GRAINS, IBR-2) of the reflected beam of unpolarized neutrons at the interface of the aqueous magnetic fluid (magnetite/sodium oleate/D_2O) with silicon in the coordinates "height of the detector Z - time of flight"; (b) Reflectivity as a function of the momentum transfer for the system magnetic fluid/silicon crystal measured in configurations 'crystal on top' and 'crystal at bottom' with corresponding representations of the structural organization of nanoparticles of the magnetic fluid at the interface with silicon.

Using small-angle neutron scattering, changes in the structural organization of transformer-oil-based magnetic fluids have been observed under the action of an external DC and AC electric field (**Fig. 6**) [8]. The investigations have been carried out to clarify the effect of the voltage breakdown enhancement in liquid transformers when adding nanoparticles, specifically magnetite nanoparticles stabilized by oleic acid, to a liquid carrier. It has been shown that after the application of a DC electric field along with a macroscopic phase separation the aggregation at the size level of 100 nm takes place strongly dependening on the field strength. After the electric field is switched off, after a time (of the order of a few hours) the system returns to its original structural state. In the case of an AC electric field, the aggregates also appear at sufficiently low frequencies, and the process terminates when the frequency exceeds a certain critical value. Thus, in addition to the effects of aggregation in an external magnetic field, which is typical for magnetic fluids, a similar sensitivity to the electric field for magnetic fluids based on dielectric carriers has been detected, which opens up new potential possibilities for regulating the properties of these complex systems using external control parameters. The study has been carried out in collaboration with the Institute of Experimental Physics, Slovak Academy of Sciences (Kosice, Slovakia), Faculty of Physics of the Taras Shevchenko National

University of Kiev (Kiev, Ukraine), and the Research Centre of Jülich - Department of Neutron Research (Munich, Germany).

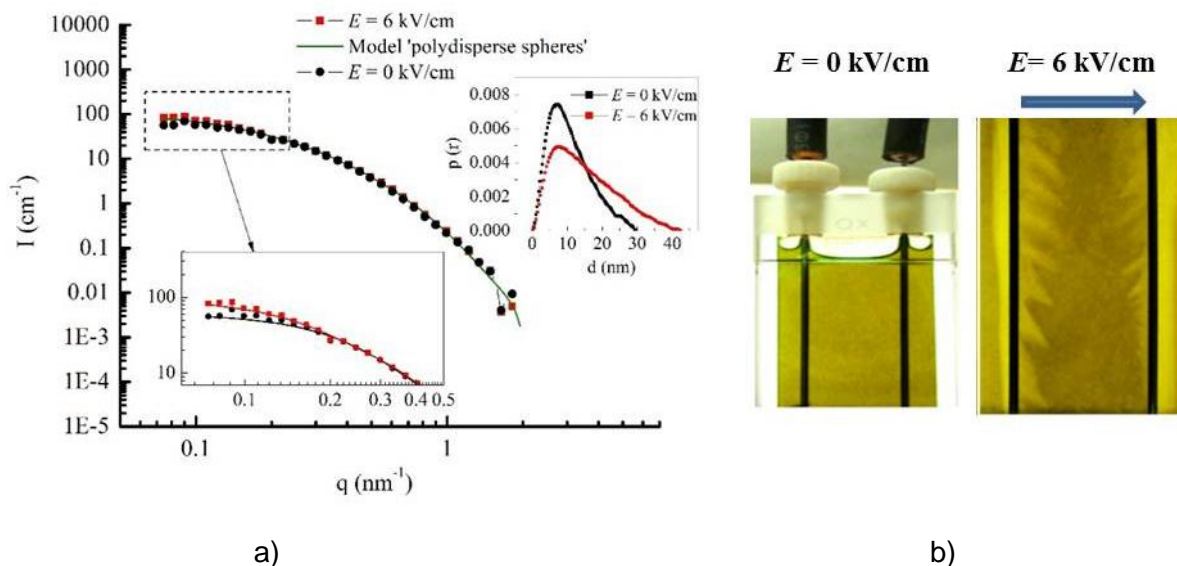a)   b)

Fig. 6. The effect of an external electric field on the structure of the magnetic fluid magnetite/oleic acid/transformer oil for (a) nanoscale: small-angle neutron scattering (YuMO, IBR-2), magnetite concentration of 1%, and (b) macrolevel: visual observation of phase separation in a quartz cell (1 mm thick), magnetite concentration of 0.05%. The inset in (a) shows the correlation functions reconstructed from the scattering curves (in the form of pair distance distribution functions) for a fluid in two states: "without a field" and "in a field", which point to an increase in the characteristic size as a result of aggregate formation under the applied field, as well as the presence of anisotropy in the aggregate shape.

Molecular dynamic (MD) simulations of the low-polarity organic solutions of saturated mono-carboxylic acids with alkyl chain lengths C14 (myristic acid) and C18 (stearic acid) used in the stabilization of magnetic fluids have been applied for the interpretation of the experimental curves of small-angle neutron scattering (SANS) from these systems [9]. In particular, the comparison of the acid structural parameters obtained in the analysis of the SANS curves from the solutions in deuterated benzene and decaline has revealed that in the second solvent there is a significant (up to 15%) increase in the limiting partial volume of the acid molecules despite their close effective conformational lengths. Thus, it has been found that the considered C14 and C18 acids due to the rapid attenuation of the dispersive interaction with distance are characterized by a lower affinity (lyophilic properties) to decalin which exhibits a more complex structure as compared to benzene. Also, the formation of a liquid crystalline phase in concentrated solutions (concentration ranges of 7 – 25 vol.% for C14 and 3 - 10 vol.% for C18) based on deuterated solvents has been considered. The lower values observed in the experiments for the formation of the liquid crystal phase in the solutions based on decalin as compared to benzene can be explained by the structural features of the solvate shells around the acids obtained from the MD simulations. The study has been carried out in collaboration with the Wigner Research Centre for Physics of the Hungarian Academy of Sciences (Budapest, Hungary) and Faculty of Physics of the Taras Shevchenko National University of Kiev (Kiev, Ukraine).

1. SCIENTIFIC RESEARCH

1.3. Investigations of carbon nanomaterials

Small-angle neutron scattering has been applied to characterize the structure of commercial aqueous dispersions of detonation nanodiamonds (DND) [10]. It has been found (**Fig. 7**) that the fractal organization of clusters in the solutions repeats the results of the previous similar experiments on the DNA dispersions of different types, which is indicative of a unique mechanism of the cluster formation during the dispersion synthesis. To explain this mechanism, a modified model of diffusion-limited aggregation (DLA-model) extended for the first time to the case of clusters of polydisperse structural units (DNA particles) has been proposed. It has been shown that along with the polydispersity of DNA particles a sufficiently high polydispersity of the clusters is required to fit the scattering curves by this model. The "light" and "heavy" cluster fractions separated by centrifugation reveal the same kind of clusters at different size scales. The effect of the scattering structure-factor characterizing the cluster-cluster interaction in concentrated suspensions of "light" and "heavy" cluster fractions has been described. The study has been carried out in collaboration with the Department of Chemistry of the Moscow State University (Moscow, Russia) and the Faculty of Physics of the Taras Shevchenko National University of Kiev (Kiev, Ukraine).

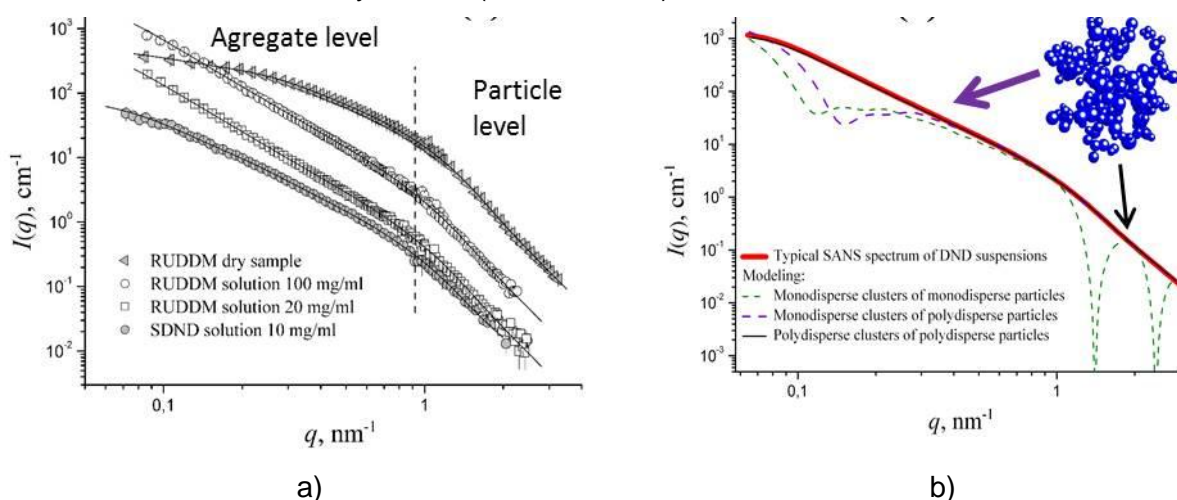a)   b)

Fig. 7. (a) Experimental curves of small-angle neutron scattering (YuMO, IBR-2) from commercial aqueous dispersions of detonation nanodiamonds, RUDDM (Real-Dzerzhinsk Ltd.) and SDND (PlasmaChem GmbH), are compared with the model curves (solid lines) calculated in the exponential/power-law approximation for the two structural levels (indicated in the graph). (b) Calculated curves of small-angle scattering for the model of diffusion-limited aggregation with monodisperse/polydisperse structural units and monodisperse/polydisperse clusters are compared with the curve calculated in the exponential/power-law approximation with the parameters obtained from the analysis of experimental data.

Complex investigations (including UV-Vis spectrometry, atomic force microscopy, small-angle neutron and X-ray scattering, dynamic light scattering) of mixtures of aqueous solutions of fullerene C60 (obtained by the solvent substitution method) with antitumor antibiotics cisplatin [11] and doxorubicin [12] have been carried out. The formation of complexes of C60 with antibiotics has been revealed and confirmed by complementary quantum mechanical calculations. From the studies performed in collaboration with the Faculty of Biology of the Taras Shevchenko National University of Kiev (Kiev, Ukraine), it has been concluded that these complexes are responsible for the enhanced anticancer effect of fullerene-antibiotic mixtures as compared to pure antibiotics. It has been assumed that in this case the fullerene improves targeted delivery of antibiotics, promotes antibiotic

accumulation in tumor tissues and increases the duration of drug exposure on tumors, thereby reducing toxic effects of anticancer drugs on vital organs.

In the framework of the research of cluster formation in fullerene solutions the kinetics of dissolution of C60 in a polar solvent, N-methyl-2-pyrrolidone (NMP), has been studied by varing temperature and speed of the component stirring during the preparation of the solution [13]. This system is characterized by a transition from a molecular solution to a colloidal solution, whose detailed description is of great interest from both fundamental and practical viewpoints. Based on the proposed model of the evolution of the C60/NMP solution, as a result of the competition between dissolution and complex formation, a diagram of the corresponding rates depending on the conditions of the solution preparation has been plotted (**Fig. 8**).
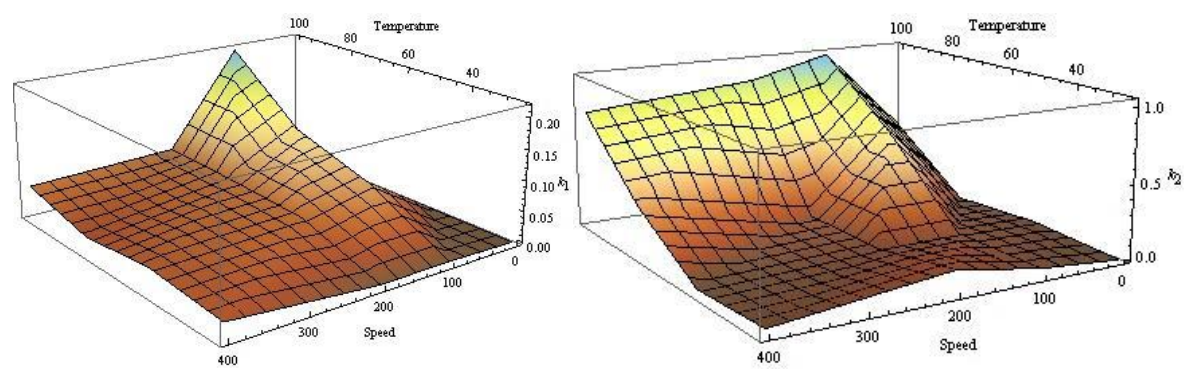

Fig. 8*. Diagram of the rates of dissolution (k1) and complex formation (k2) in C60/NMP solution (concentration 0.3 mg/ml) depending on the stirring speed and temperature. The speed values have been obtained from the analysis of the absorption peak intensity in UV-Vis spectra at a wavelength of 330 nm.*

1.4. Investigations of layered nanostructures

Neutron studies on the modification of the magnetic state in the ferromagnetic layered nanostructure $Ta/V/Fe_{0.7}V_{0.3}/V/Fe_{0.7}V_{0.3}/Nb/Si$ under the influence of superconductivity were continued (**Fig. 9**).
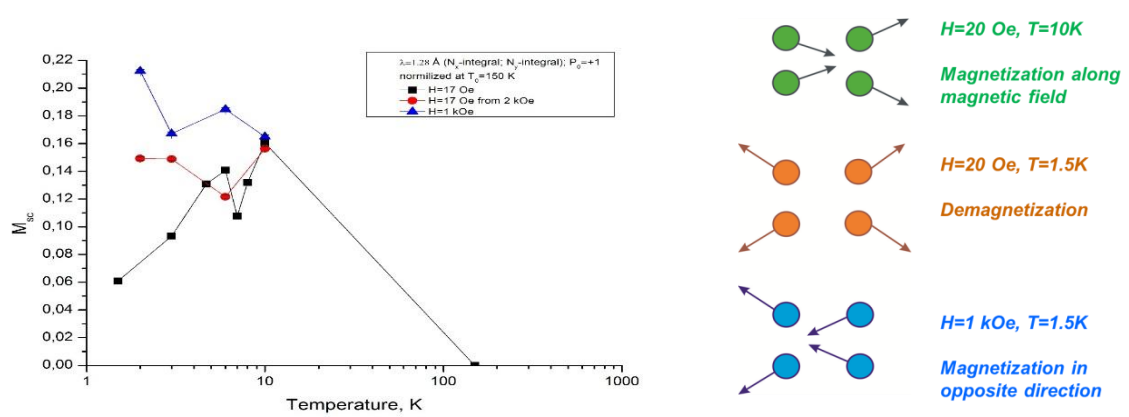

Fig. 9*. Temperature dependences of neutron scattering from magnetic clusters in ferromagnetic layered nanostructure $Ta/V/Fe_{0.7}V_{0.3}/V/Fe_{0.7}V_{0.3}/Nb/Si$ in various magnetic fields (left) and a schematic representation inllustrating the behavior of the magnetic moments of the clusters (right).*

1. SCIENTIFIC RESEARCH

In the temperature range of 1.5-8 K where niobium and vanadium layers are superconducting, different temperature dependences of neutron scattering from the clusters in this magnetic nanostructure have been detected for the cases of (i) structure in a weak magnetic field of 20 Oe, (ii) structure with residual magnetization after magnetization in a field of 2 kOe, and (iii) structure in a constant magnetic field of 1 kOe. This indicates that the influence of superconductivity on the state of the magnetic clusters in the layered structure depends on the magnetic field strength. Using the real time reflectometry the temperature dependences of neutron scattering have been measured. They showed a characteristic relaxation time within several tens of minutes for the magnetic state of the layered structure Ta/V/Fe$_{0.7}$V$_{0.3}$/V/Fe$_{0.7}$V$_{0.3}$/Nb/Si. The dependences associated with the creep of the magnetic flux in the magnetic non-superconducting structure and oppositely directed creep in the superconducting structure have been observed.

1.5. Investigations of biological nanosystems, lipid membranes and complexes

An ability to separate cells from the environment is one of the most important functions of biological membranes. The violation of the membrane integrity causes the cell death. However, local and short-term changes in the membrane integrity leads to the creation of a new structure by cell fusion/fission. Fusion is the basis of the most important physiological processes such as exocytosis, secretion, formation of secondary lysosomes. In addition, *in vitro* targeting cell fusion by various fusion agents is widely used to solve a number of problems in biomedicine and biotechnology. Dimethyl sulfoxide (DMSO) is one of the fusion agents. In the presence of DMSO, pores in membranes appear, thereby increasing permeability and reducing stiffness of the membrane, which in turn initiates the fusion process. DMSO is toxic to living cells. Diethyl sulfoxide (DESO) is less toxic than, for example, DMSO and glycerol, to *E. coli*. Apparently, the mechanism of the interaction of DESO and DMSO with biological membranes is identical. The SANS analysis of the influence of the DMSO and DESO concentration on structural and phase transitions in phospholipid membranes has been carried out. It has been shown that fusion occurs at a lower molar concentration for DESO than for DMSO. DESO (like DMSO) increases the temperature of the main phase transition (T_f). However, in the presence of DMSO the phase transition occurs at a lower temperature ($T_f = 35.2°C$ and $33.6°C$) and in a narrower temperature range than in the presence of DESO at the same molar concentration of sulfoxides.

The process of the spontaneous formation of phospholipid vesicles in the presence of calcium ions has been studied by small-angle neutron scattering. For the first time, the behavior of the intermembrane distance in a transitional region for membranes in both liquid and gel phases has been investigated in detail. It has been shown that the transition of a system from the bound state to the unbound state in both phases is of continuous character. If for the liquid phase this result predicted in many theoretical works was expected, the data obtained for the gel phase contradict most of the previously published works. The theoretical investigations concerning the gel phase indicate that the addition of calcium ions to multilayered lipid membranes should cause for the membranes a sharp transition from the bound state to the unbound state, since there are no ondulations in the gel phase (membrane is "harder" than it is in the liquid phase). However, our studies have shown that the influence of the ondulation forces on the membrane interaction shoud be taken into account. Thus, our experimental results confirm the hypothesis of R. Lipowski (1986) about a possible continious character of the transition. The critical concentrations of calcium ions (0.3 mM for the gel phase and 0.4 mM for the liquid phase) when the analyzed transition takes place have been obtained. In addition, the binding constants for calcium ions with lipid membranes (22 M-1 in the gel phase and 24 M-1 in the liquid phase) have been determined.

The visual pigment rhodopsin is a typical representative of the vast family of receptors coupled to G-proteins (GPCR). GPCR in membranes function in dimeric or oligomeric states. However, for rhodopsin and for the whole A class of rhodopsin-like GPCR the functional role of the dimeric state has not yet been established. A supramolecular organization of rhodopsin in photoreceptor membranes is currently much debated. The structural organization of the photoreceptor membranes has been investigated by small-angle neutron scattering with the contrast variation (**Fig. 10**).
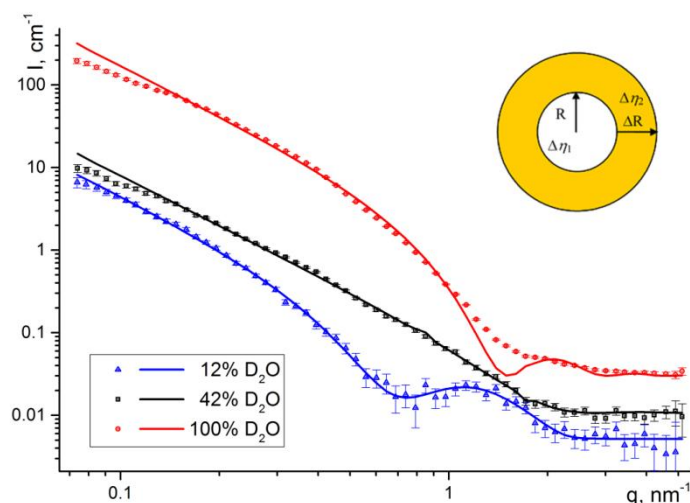

Fig. 10. Small-angle neutron scattering curves from a photoreceptor membrane measured with the contrast variation.

It has been found that rhodopsin has an unusually high packing density in the photoreceptor membrane with the distance between protein molecules of about 56 Å [14]. With a high probability the data obtained assume a monomeric character of rhodopsin molecules in the photoreceptor membrane.

1.7. Atomic and molecular dynamics

In recent years, much interest has been shown in the study of hydrogen-bonded, donor-acceptor type supramolecular co-crystals for their potential use as functional materials with semiconducting and/or ferroelectric properties arising due to the electron- and proton-transfer phenomena. A comprehensive study of the crystal structure and molecular dynamics of co-crystals of bromanilic acid with 2,6-dimethylpyrazine (BrA: 2,6-DMP) 1:1 has been carried out using the methods of single-crystal X-ray diffraction, neutron spectroscopy (NERA spectrometer) and complementary spectroscopic methods, **Fig. 11**. [15]. To interpret the experimental results, theoretical calculations have been performed as well.

The structural analysis has revealed that the system under study crystallizes in the monoclinic P21/c space group, with four molecular units per unit cell. The crystal structure can be described as an infinite net of antiparallelly oriented hydrogen bonded molecular chains (**Fig. 11**). The intermolecular analysis has revealed the nonequivalency of the moderate strength hydrogen-bonding interactions and the presence of multiple specific intermolecular forces. The theoretical calculations using Hirschfeld surface approximation and reduced density gradient approaches have exposed the role of stacking interactions and weak van der Waals forces in the stabilization of the crystal structure.

1. SCIENTIFIC RESEARCH

The analysis of vibrational properties was performed using the methods of neutron and optical spectroscopy (mid-, far- and terahertz ranges).
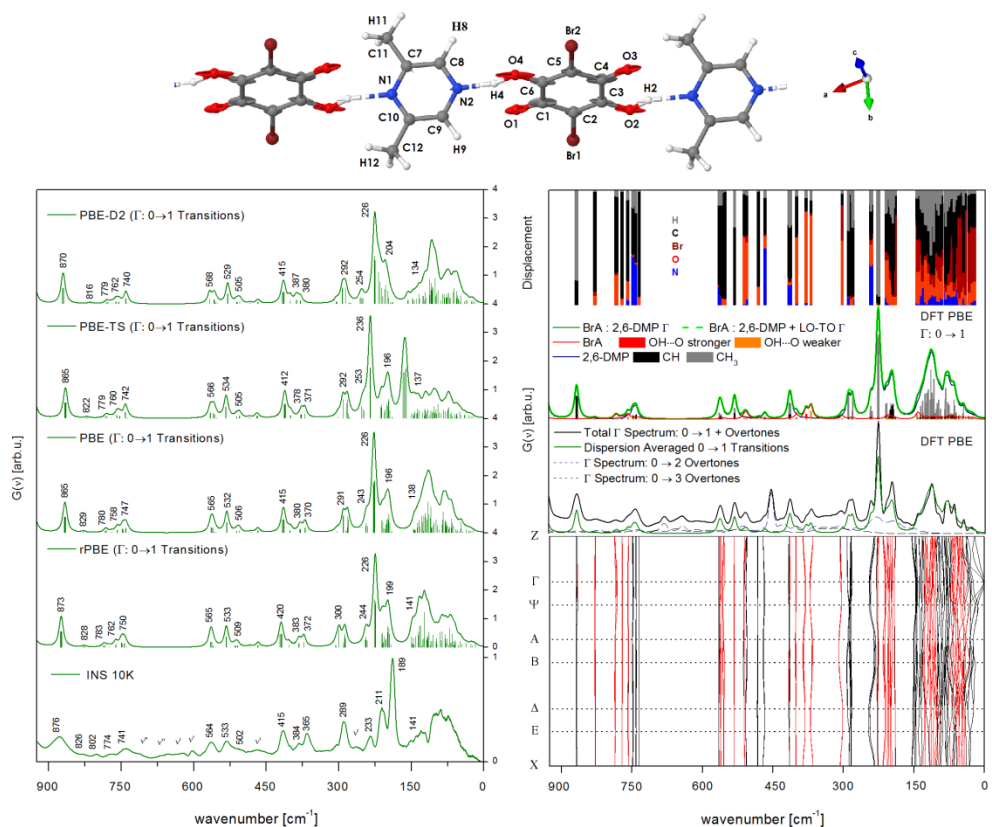

Fig. 11. Molecular structure, inelastic neutron scattering spectra (NERA 10K) and theoretical calculated vibrational spectra (for 0 → 1 transitions) of BrA:2,6-DMP (1:1) in the frequency range below 925 cm^{-1}. The theoretical spectra are given for both constrained (rPBE; PBE) and fully (PBE-TS; PBE-D) optimized crystal structures. Also, calculated phonon dispersion curves along with the vibrational density of states decomposed into partial density contributions of each molecular fragment are selectively presented. In addition, the dispersion averaged spectrum is given along with the total Γ-point spectrum including the overtone contributions.

The theoretical analysis of the vibrational spectra was made in the framework of DFT in the semilocal approximation taking into account semiempirical van der Waals corrections. Despite the quasiharmonic approximation, good agreement between the theoretical and experimental spectra was achieved. In particluar, the significant influence of the long-range dipole coupling on the IR spectrum and the effect of the structure on the vibrations with small wave numbers have been revealed.

1.8. Applied research

Among traditional applied investigations in the NICM Department are the experimental studies of internal stresses and texture of rocks and minerals, determination of internal stresses in bulk materials and products, including engineering materials and components of machines and devices. For the most part, these investigations are carried out using neutron diffraction.

On the FSD diffractometer the experiments have been continued on the investigations of distributions of residual stresses in welds that are induced by various beam welding methods (**Fig. 12**). The investigations have been carried out in cooperation with the Institute of Electronics, BAS (Sofia, Bulgaria). Residual stresses in a toothed gear of a sports car transmission gearbox after electron beam welding have been studied. It has been found that in the weld region and adjacent heat-affected zone (HAZ) the residual stresses and microstrains have minimum values. In the region remote from the weld the residual stresses are rather large, and their maximum levels reach values of about 500 MPa, which may point to non-optimal parameters of the beam welding.

a)   b)
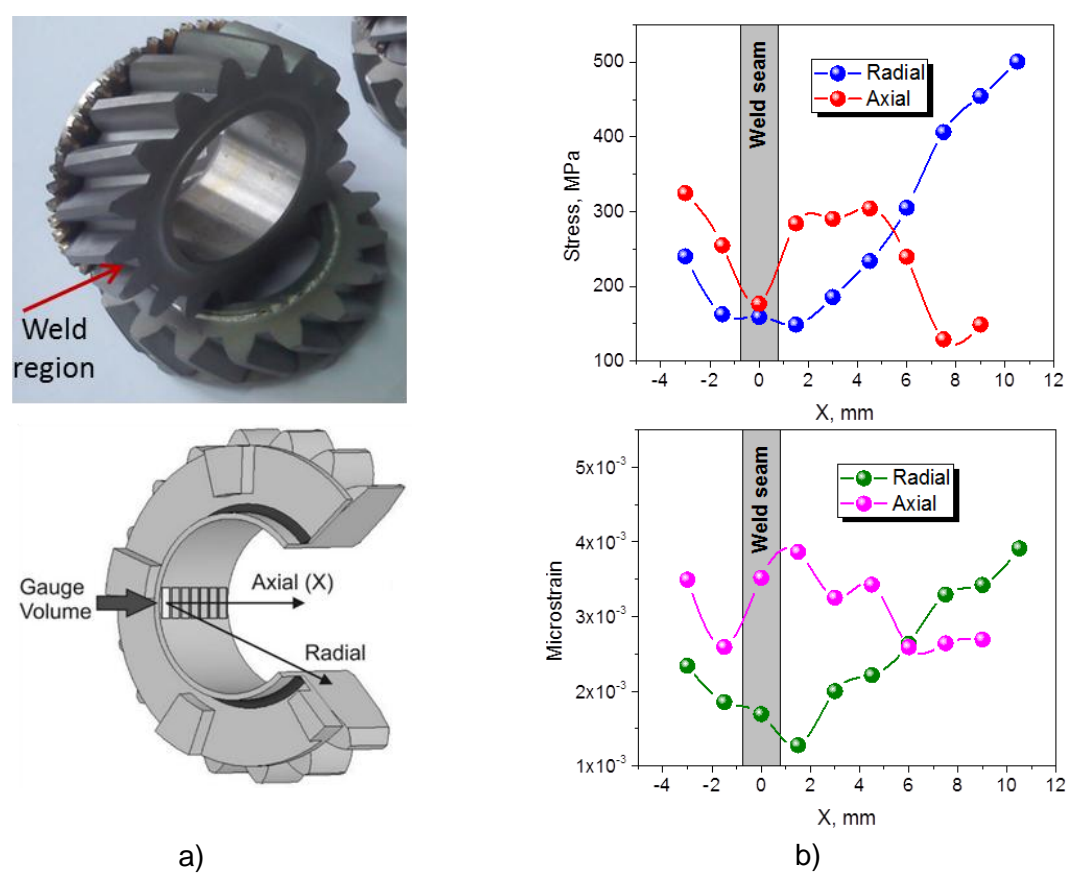
Fig. 12. a) Photo of toothed gears welded by electron beam welding and scheme of the measurement of residual stresses in the toothed gear. b) Distribution of residual stresses (top) and microstrains (bottom) in the toothed gear welded by electron beam welding.

A detailed study of residual stresses has been performed for a plate of size 100x100x10 mm of structural steel S355J2+N welded by laser beam welding (**Fig. 13**). The distribution of residual stresses along the scan coordinate X is of an alternating character, and the maximum-largest is the component of the stress tensor σ_x (~ 400-460 MPa) directed along the weld line and having mainly stretching character in the heat-affected zone. The analysis of the behavior of the peak widths near the weld has shown that the peak broadening depends on the direction [hkl] in the crystal, which is a typical manifestation of the orientation factor of dislocations in respect to the scattering vector. In the given sample the maximum level of microstrains in the material reaches $4.8 \cdot 10^{-3}$, and the position of the maximum in the microstrain distribution coincides with the location of the weld center. Using the obtained data on microstrains the dislocation densities in the material have been calculated.
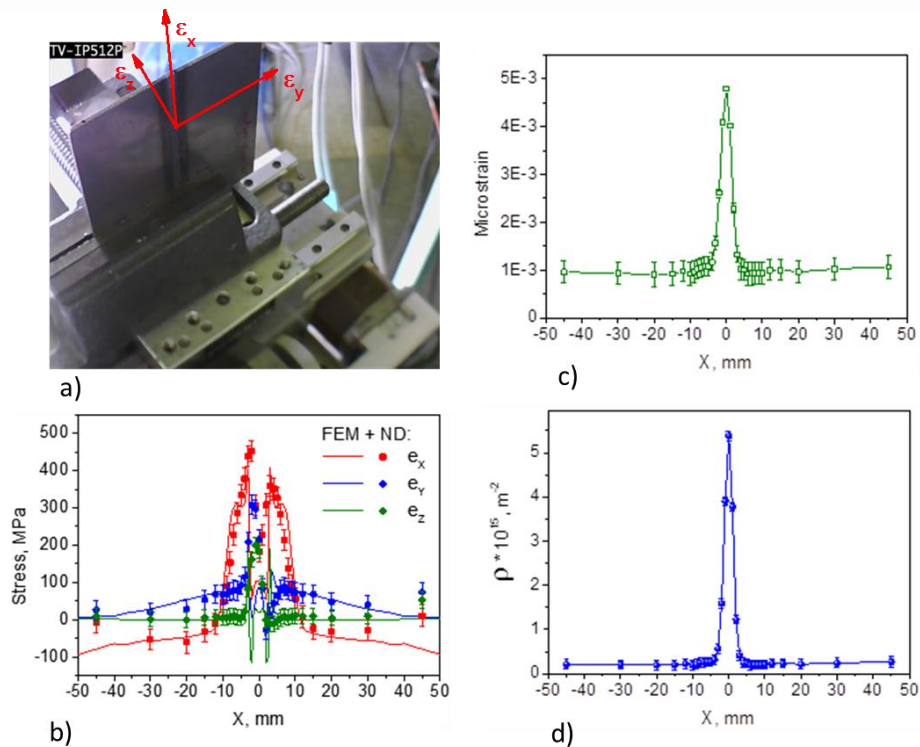
1. SCIENTIFIC RESEARCH

Fig. 13. The sample under study (plate welded by LBW) during the experiment at FSD (a). The arrows indicate the strain tensor components. Experimentally measured distribution of residual stress tensor components in the plate (symbols) welded by LBW (b). For comparison, the results of numerical simulation using the finite element method FEM (solid lines) are presented. Distribution of microstrains in the crystal lattice (c) and dislocation densities (d) obtained from the diffraction data in the plate welded by LBW.

In addition to the neutron diffraction experiments and in the framework of the existing cooperation numerical calculations have been performed by the finite element method - FEM (group of Prof. V.Mikhailov, Brandenburg University of Technology, Germany). The comparison of the neutron data and calculations using FEM shows a good agreement, which supports the validity of the developed theoretical model of the laser welding process. This information can serve as a basis for developing specific technical recommendations to achieve the desired level and profile of residual stresses.

On the SKAT/EPSILON diffractometer *in situ* deformation experiments have been conducted with a granite sample from the Forsmark region (Sweden) containing quartz, plagioclase and biotite. A cylindrical sample (d = 30 mm, l = 60 m) was subjected to cyclic uniaxial loading in the range from 20 to 140 MPa. The measurements were conducted at 7 load levels, for each level the sample was reloaded. Applied and internal stresses were determined from the shift of the diffraction lines in the range of up to d = 5.1 Å. In addition, the acoustic emission measurements have been carried out, the combination of which with neutron experiments is needed for better understanding of reasons for the Kaiser effect. The quartz texture in the granite sample is well developed and characterized by one maximum in the pole figure [0001] near the z-axis and 120° pole density distribution of other lattice directions around the [0001] cluster (**Fig. 14**). This gives grounds to suggest post-kinematic crystallization. In contrast, the texture of other phases is very weak (**Fig. 14**).
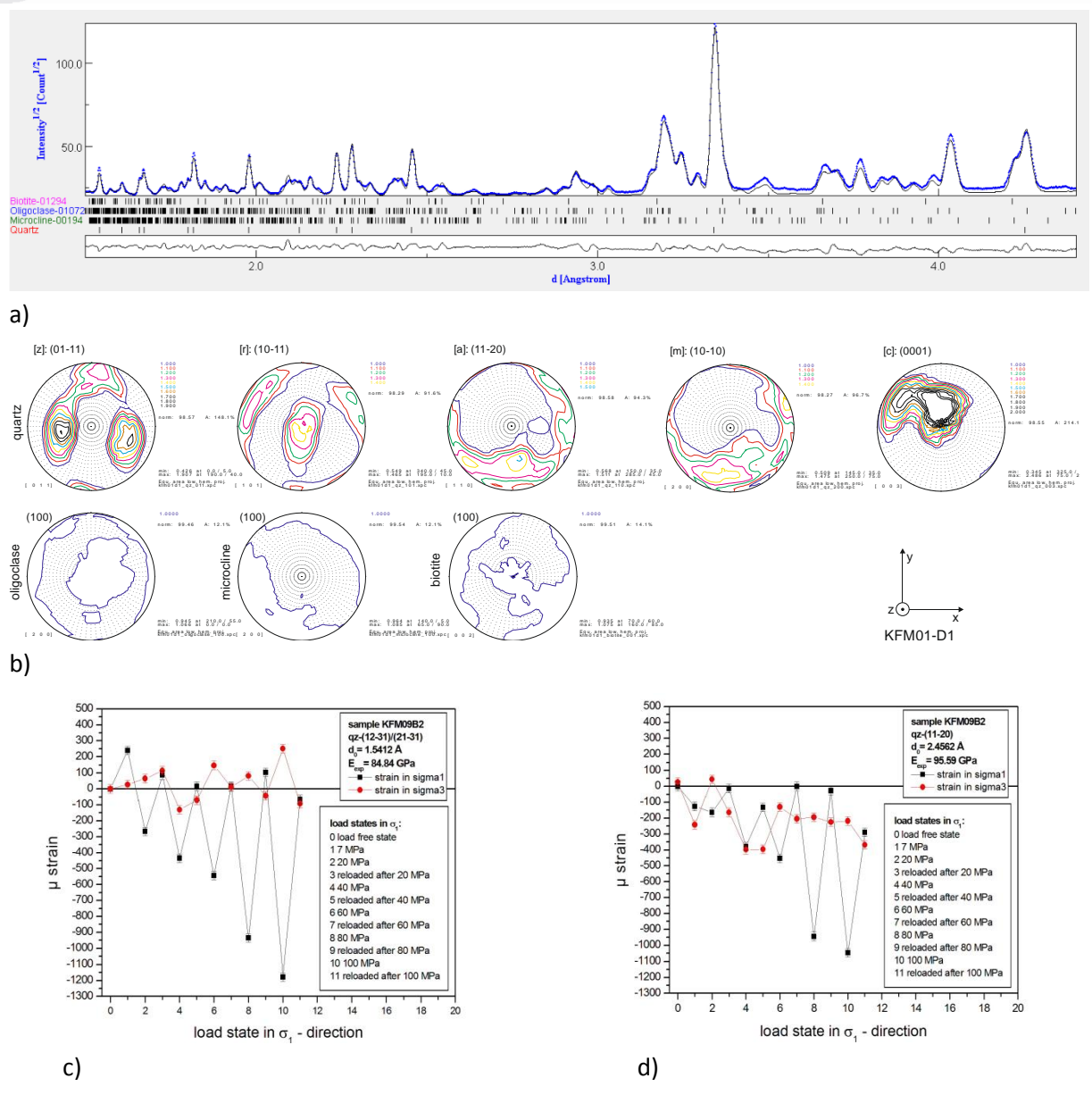
a)

b)

c)

d)

Fig. 14. *Normalized TOF neutron diffraction spectra of granite sample obtained with the SKAT diffractometer. The Figure shows the experimental points (blue) and calculated profiles (black) as well as the positions of the diffraction peaks calculated by the MAUD program (a). Textures of quartz (top), oligoclase, microlin and biotite (bottom) (b). Applied and internal stresses of quartz (12-31) and (11-20) (c, d).*

The measured internal stresses were compared for the milled (< 62 μm) and annealed powder of the sample without stresses. During the internal stress measurements the cylindrical sample under study was rotated around the *z* axis with a step of 15° in the *xy* plane. The measured residual stresses were in the range from -1×10^{-3} to 1.2×10^{-3}.

On the EPSILON diffractometer the experiments have been conducted to determine the magnitude and distribution of internal stresses caused by tensile embrittling destruction in the course of phased "Brazilian" creep tests for a pure marble sample (>95% $CaCO_3$). A comparison of internal

1. SCIENTIFIC RESEARCH

stresses measured before and during phases of mechanical loading has been made. The obtained data are important for studying the mechanisms of rock destruction.

The internal stresses occurring as a result of elasto-plastic deformation and residual stresses after removing the mechanical load in metal-matrix composite alloys Al/SiC$_p$ have been studied by neutron diffraction (EPSILON diffractometer) and synchrotron radiation techniques. The experimental results were compared with the elasto-plastic deformation model to determine the parameters responsible for the deformation of the Al matrix — critical allowable shear stress and hardening parameter. The analysis of data has shown that during the tensile test the Al matrix undergoes plastic deformation, and the SiC phase remains elastic. A self-consistent model allows one to correctly predict stresses in the SiC phase, but it overestimates the calculated values of the lattice strains in the Al matrix, which can be connected with the initial thermal stresses.

On the SKAT diffractometer the texture in a number of samples of high-strength vessel steels has been studied by thermal neutron diffraction (**Fig. 15**).
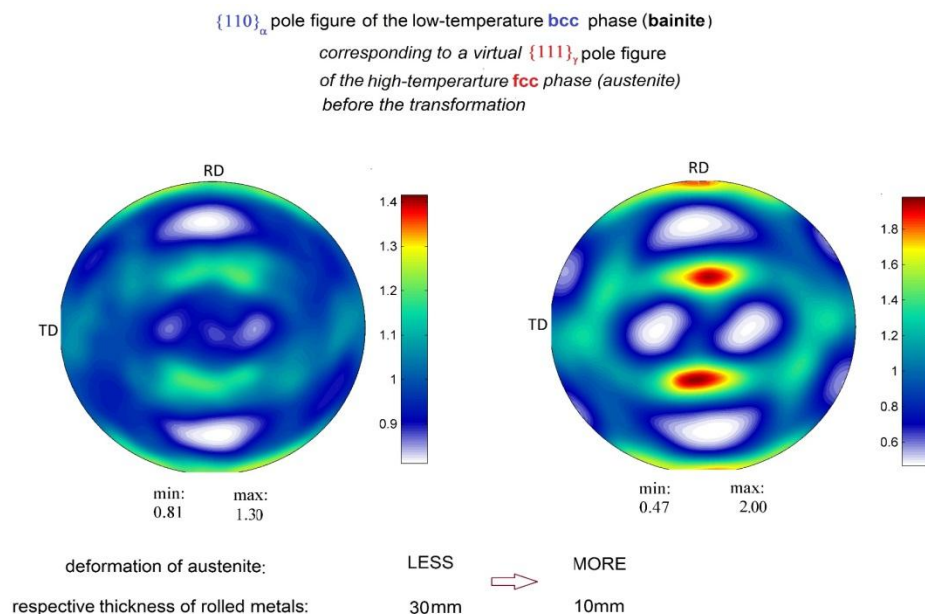

$\{110\}_\alpha$ pole figure of the low-temperature **bcc** phase (**bainite**)

corresponding to a virtual $\{111\}_\gamma$ pole figure
*of the high-temperarture **fcc** phase (austenite)*
before the transformation

Fig. 15. Pole figures of low-temperature bainite phase with a bcc structure.

The inhomogeneity of the texture across the thickness of a steel slab was investigated. Due to a large thickness (300 mm) of the slab the crystallization proceeds under various temperature conditions, therefore a strong morphological inhomogeneity can be observed across the thickness of the material. A set of 1368 (19×72) diffraction spectra was obtained from which complete direct pole figures (PF) with a grid size of 5˚×5˚ were derived. For each sample three pole figures (200) (110) (211) for α-Fe were obtained. It was revealed that the crystallographic structure changes only slightly across the thickness of the slab. From this it follows that the change in the morphological structure across the thickness of the high-strength steel slab is not related to a change in the crystallographic texture. In addition, the texture of rolled samples with different degrees of deformation has been studied as well. It has been found that the intensity of texture increases with the degree of rolling. Pole figures have been obtained for a low-temperature bainite phase with a bcc crystal lattice. The pole figure (110) for this phase corresponds to the pole figure (111) for the virtual high-temperature

austenitic phase with an fcc lattice (typical texture of rolled copper). The high-temperature phase (austenite) is destroyed during quenching as a result of the phase transition. However, the revealed relationships between the pole figures of low-temperature (bainite) and high-temperature (austenite) phases provide an insight into the texture of the austenite destroyed during the phase transition.

II. Instrument development

Work to develop the final configuration of the new DN-6 diffractometer was continued. In cooperation with the SC Department a second ring detector consisting of 96 independent helium counters has been manufactured. The first successful methodological and scientific experiments with a new two-detector system have been carried out (**Fig. 16**).
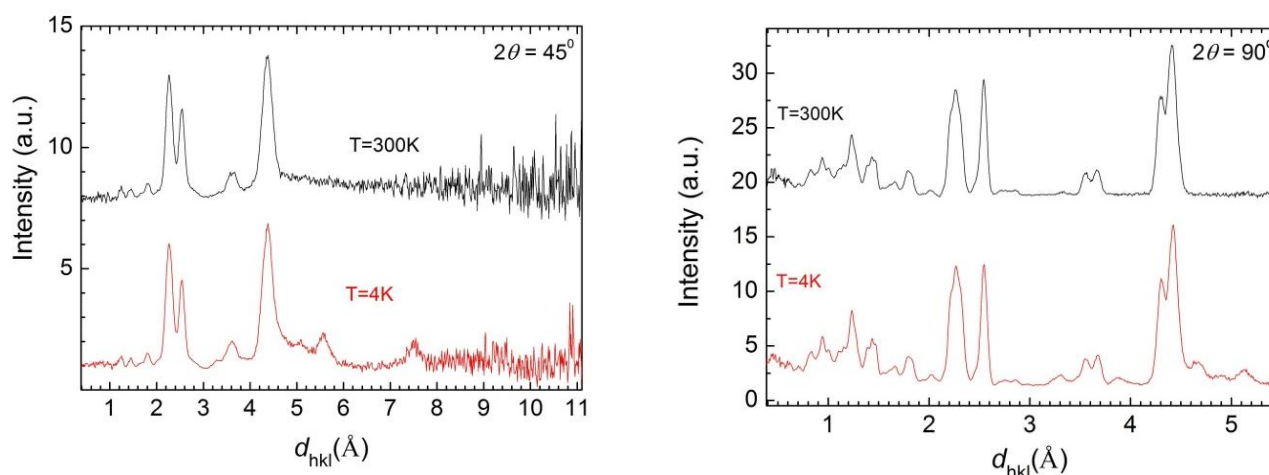
Fig. 16. Neutron diffraction spectra of $LiMn_2TeO_6$ obtained at scattering angles $2\theta = 45°$ (left) and $90°$ (right).

In 2015, the user program has started to be implemented on the GRAINS reflectometer. In accordance with the list of submitted proposals for the second half of 2015, more than ten experiments on electrochemical interfaces, magnetic colloidal systems, polymer solutions and melts, lipid solutions and others have been carried out at GRAINS. Among the interested organizations are the research centers of Russia (MSU, PNPI, NRC KI), Slovakia (IEP SAS), Ukraine (KNU), Hungary (WRCP HAS), Tajikistan (IC ASRT). In particular, the possibilities of neutron reflectometry experiments for electrochemical interfaces under potential have been considered in the framework of comprehensive studies combining various complementary methods of synchrotron radiation and thermal neutrons [16]. The main emphasis was placed on the optimization of experimental conditions (substrate, electrode, solvent) to detect the formation of a transitional layer (so-called solid electrolyte interphase, SEI) on the model electrode and to obtain its characteristics (thickness and density) depending on the applied potential. To eliminate the influence of uncontrolled oxidation of metal electrodes on the results of experiments, the regulated oxidation of titanium and nickel films deposited on a glass substrate has been investidated (**Fig. 17**). The study has been carried out in collaboration with the Department of Chemistry of Moscow State University (Moscow, Russia), Petersburg Nuclear Physics Institute, NRC "Kurchatov Institute" (Gatchina, Russia) and the Faculty of Physics of the Taras Shevchenko National University of Kiev (Kiev, Ukraine).
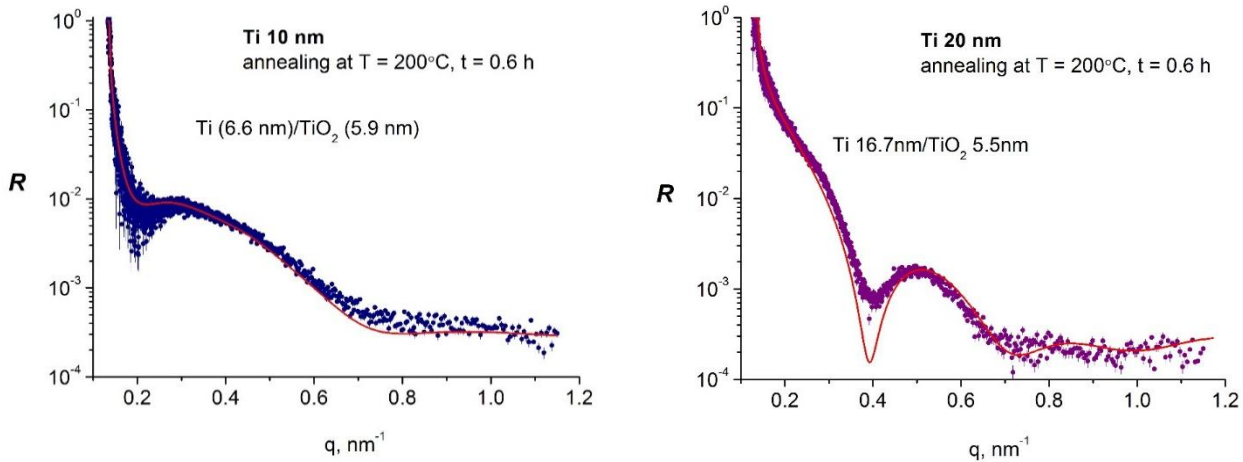
1. SCIENTIFIC RESEARCH

Fig. 17. Experimental reflectivity curves (GRAINS, IBR-2) for model metal (Ti) films of different thicknesses on a glass substrate oxidized using a special procedure (PNPI, NRC KI). The solid lines show the simulation results with the indication of the obtained thicknesses for the film and the oxide layer.

The realization of the project aimed at creating a basic configuration of the diffractometer on beamline 6a for neutron diffraction studies of transition processes in real time (RTD diffractometer - Real Time Diffractometer) has been completed. The diffractometer (**Fig. 18**) is designed to study irreversible transition processes with characteristic times ranging from fractions of a second to tens of minutes.
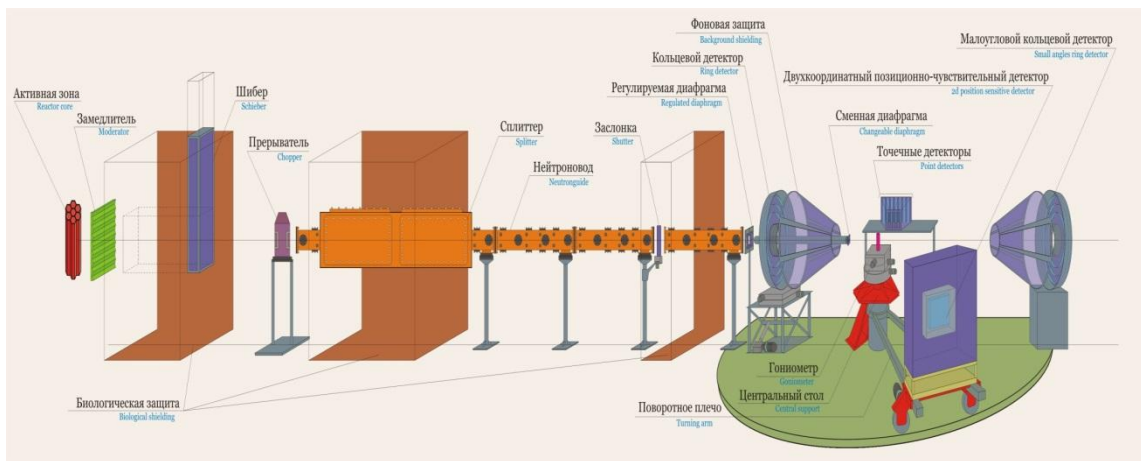

Fig. 18. Basic components of the RTD refractometer at the IBR-2 reactor. Shown from left to right are: reactor core and moderator, biological shielding, chopper to reduce the background between the reactor pulses, splitter" to split the neutron beam into two beams, mirror neutron guide with a shutter to shut the beam, adjustable diaphragm at the exit of the neutron guide, central platform with a sample position and detectors. Four detector units are used: 2D PSD on a rotating platform, two ring detectors at small and large scattering angles and a battery of ^{3}He-counters near $2\theta = 90°$.

In favorable cases, the time resolution of RTD will be fractions of a millisecond. The developed detector system (small-angle detector, detectors at medium scattering angles of 30° - 90° and a

2015

Annual Report

detector at large scattering angles in combination with the available wavelength range of 0.5-20 Å) makes it possible to obtain diffraction spectra over a wide range of interplanar spacings (d_{min}, d_{max}) = (0.5 - 300) Å. A triaxial goniometer and two-coordinate PSD with an active area of 225x225 mm and spatial resolution of 2x2 mm are used for investigations with single crystals and multilayer structures.

On the HRFD diffractometer the available model cell and its assembling/filling procedure have been improved. The work on the development of the cell (**Fig. 19**) based on silicon screens and multi-layer pouch-cell-type arrangement of electrode materials has been completed and first successful experiments have been conducted. The main components are: PTFE frame (white), material under study, silicon plate for incoming and scattered neutron beams, boron nitride to reduce the scattering from the cell components. The cell design allows easy assembling in an argon box, ensures good sealing and low incoherent neutron scattering from the cell screens.
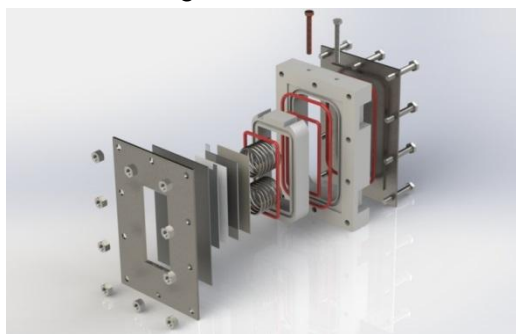

Fig. 19. Schematic diagram of a new electrochemical cell.

Also, on HRFD the operation of a specialized high-temperature furnace (ILL standard) designed to heat samples up to 1100°C and for a short time up to 1300°C has started. The furnace has vanadium heaters, vanadium and aluminum screens, water cooling, two K-type thermocouples, various protection mechanisms for emergency cases. An example of diffraction spectra obtained using the new furnace for Fe-27Ga alloys is shown in **Fig. 20**.
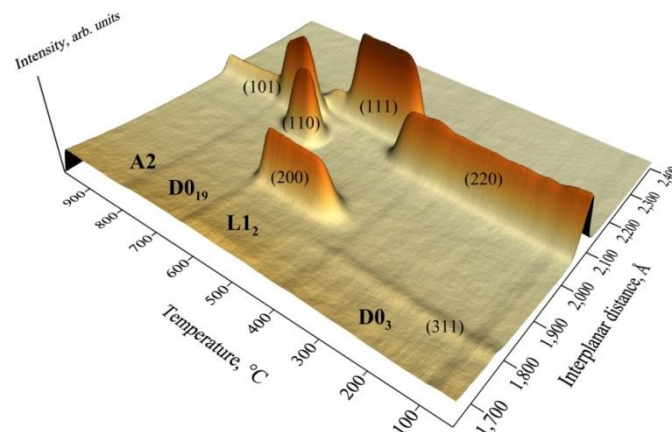

Fig. 20. Evolution of diffraction spectra obtained during heating of Fe-27Ga alloy from room temperature to 980°C at a rate of 2.25°C/min. There can be observed a sequence of structural phase transitions: D03 → L12 → D019 → A2 (standard designations of main structural types). Shown are the Miller indices of the observed diffraction peaks.

At FSD a uniaxial mechanical testing machine LM-20 has been installed, which significantly expands the range of possible experiments with the diffractometer. This device is intended to study

1. SCIENTIFIC RESEARCH

samples at an external uniaxial load directly in the neutron beam. In 2015, several test neutron diffraction experiments with the application of tensile and compressive loads on austenitic and ferritic steel samples were successfully performed at FSD (**Fig. 21**). In the autumn of 2015 first experiments with a testing machine LM-20 began to be performed on the request of external users. In future, this device is planned to be used at FSD on a regular basis.
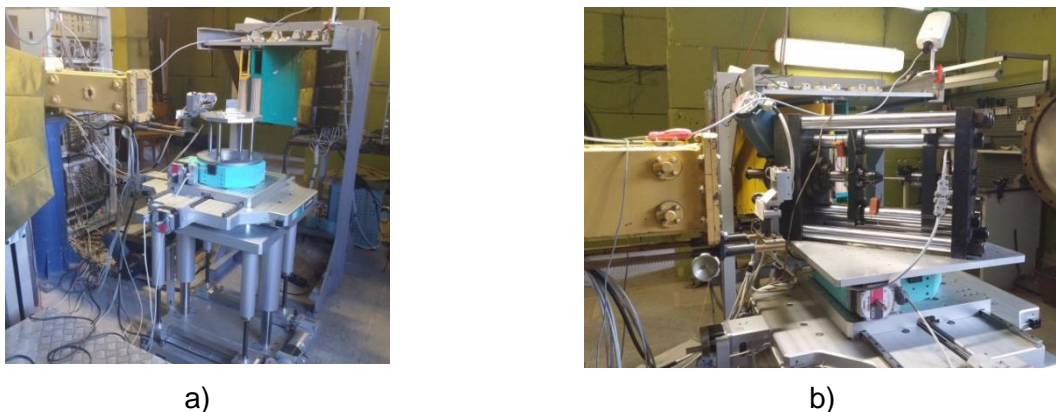

a)   b)

Fig. 21. FSD Fourier diffractometer on IBR-2 beamline 11: a) sample position on the HUBER goniometer; b) testing machine LM-20 with a steel sample.

On IBR-2 beamline 13 the work on the development of a Fourier diffractometer FSS is in progress in cooperation with the SC Department (**Fig. 22**).

Fig. 22. Fourier-diffractometer FSS on IBR-2 beamline 13 (from top to bottom and from left to right): operational control boxes of a shutter and beam stopper; entrance door to the bunker (beam exit location); glass mirror neutron guide sections before installation in a housing; neutron guide installed in a steel housing and control electronics of the Fourier chopper; experimenter's control cabin mounted on the biological shielding of beamlines № 13-14.

In 2015, operational control boxes of a shutter and beam stopper, light alarm system, power supply and control system of the Fourier chopper were installed, an experimenter's control cabin was mounted, and a mirror neutron guide in the steel casing was assembled with the participation of specialists from PNPI. In November 2015, at FSS the first trial opening of the beam was held, during which radiation conditions on the beamline were evaluated, neutron beam profiles were obtained and first diffraction spectra were collected.

A spin neutron interferometer of a new type based on the splitting of neutron waves reflected from a magnetic mirror has been studied. In the setup an initially unpolarized neutron beam passes through a system of two mirrors placed in a perpendicular magnetic field. A precession of the neutron magnetic moment as a periodic wavelength dependence for the intensity of neutrons passing through the system of two magnetic mirrors has been observed (**Fig. 23**). With increasing magnetic field up to 200 Oe the precession of the neutron beam polarization decays because of magnetic field inhomogeneities. The interferometer can be a part of a spin-echo spectrometer where the influence of magnetic field inhomogeneities and neutron beam divergence are eliminated. In particular, it can be used to study a static inhomogeneous state with a micron-size correlation length and the dynamics of media with correlation times at a microsecond level, as well as to measure the width of neutron wave packets.
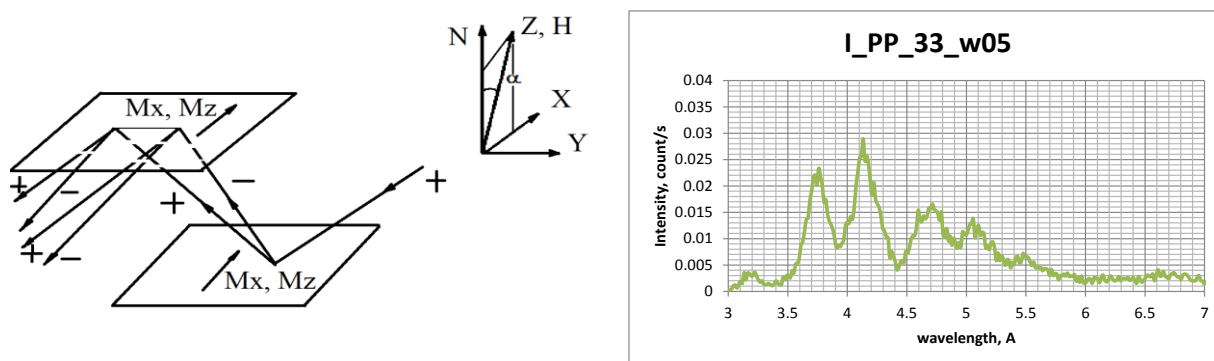

Fig. 23. Operating principle of the neutron spin interferometer of a new type (left) and spectrum of neutrons passing through the interferometer under a magnetic field of 33 Oe (right).

A method to study weakly magnetic films using the polarized neutron channeling has been developed (**Fig. 24**). The magnetic induction of a weakly magnetic layer has been measured. The structure Ta(3 nm) / $Ni_{0.67}Cu_{0.33}$(15 nm) / $TbCo_5$(150 nm) / $Ni_{0.67}Cu_{0.33}$(50 nm) / Si(substrate), in which the waveguide layer is made of a material ($TbCo_5$) with small saturation magnetization of about 200 G has been investigated. Such materials containing rare earth elements are widely used for the development of new methods for magnetic recording. However, because of the weak saturation magnetization these materials cannot be studied by standard reflectometry of polarized neutrons, which is used for materials with magnetization of more than 1000 G. In experiments, a polarized neutron beam falls at some grazing angle on a three-layer waveguide structure where the resonance amplification of the neutron wave in the average weakly magnetic layer occurs. The neutron wave phase in the resonance depends on the neutron spin direction, channel width and magnetic induction in a channel. Along with it, the grazing angles of the incident beam for spins (+) and (-) differ, and the difference in the squared sines of these angles directly gives the magnetic induction in the layer at its values of less than 100 mT. With increasing B, other factors start to determine the non-linear dependence. The prospects of this method for neutron measurements in research of weakly magnetic materials have been concluded to be good.
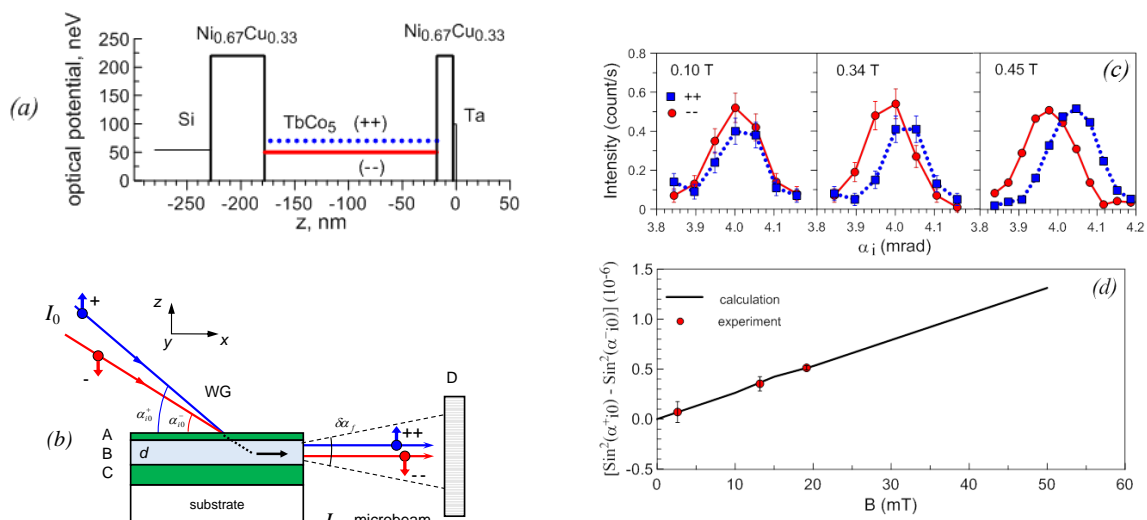
1. SCIENTIFIC RESEARCH

Fig. 24. *Optical potential profile for the nanostructure Ta(3 nm) / Ni$_{0.67}$Cu$_{0.33}$(15nm) / TbCo$_5$(150nm) / Ni$_{0.67}$Cu$_{0.33}$(50nm) / Si(substrate) (a), scheme of the experiment (b) parts of the spectrum of scattered neutrons at different magnetic fields (c) and difference of squared sines of grazing angles as a function of magnetic field induction (d).*

The operating modes of the spin-echo small-angle (SESANS) spectrometer with linearly increasing magnetic fields, which is under construction on the basis of the REFLEX reflectometer, have been numerically studied. Monte Carlo simulations of these modes for a virtual spectrometer have been performed in the VITESS software package. In particular, a program module simulating the main element of the SESANS spectrometer (spin rotator) has been created. The parameters of the model spectrometer have been chosen in accordance with the parameters of the prototype of the SESANS spectrometer being constructed on IBR-2 beamline 9. The purpose of the work was to determine the possible modes of the setup under constraction and its possibilities in the study of nanostructures. Basing on the IBR-2 parameters and the geometry of the spectrometer with respect to the location of its elements and their characteristics, it has been found that the measured correlation dependence *P(Z)* of the scattered beam polarization on the so-called spin-echo length is composed of separate intervals relating to specific spectral intervals of the neutron beam (**Fig. 25**).
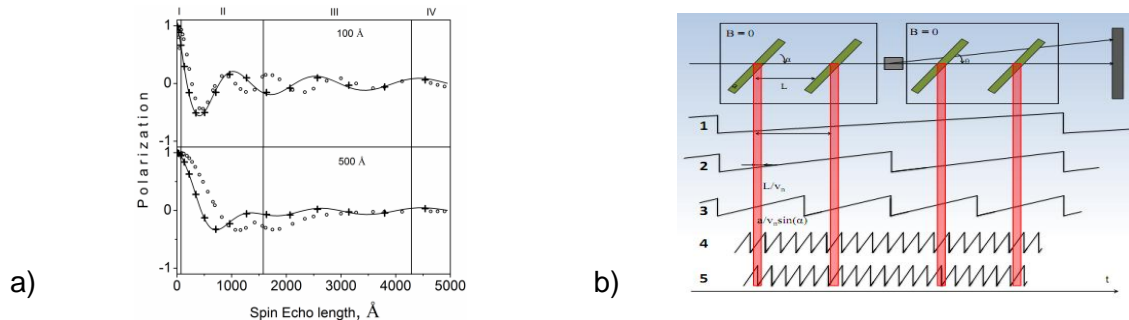

Fig. 25. *(a) SESANS signal for particles with radii of 100 Å and 500 Å. Roman numerals denote the operation modes of the instrument. The solid line and crosses designate the analytical calculations and the model scattering curve, respectively, for the ideal case of the infinite time field pulse. The circles correspond to the case of sawtooth pulses for the magnetic field realizing different modes of the spectrometer in different spectral intervals. (b) Time diagram illustrating different operating modes: one pulse of the field per passage through four (1), two (2), one (3) spin rotators; every n-th pulse per passage through one spin rotator (4).*

2015 Annual Report

Each of these intervals is characterized by its own measured correlation dependence *P(Z)*, thus, the analysis of the total correlation dependence should consist of an independent analysis of its individual parts.

On the YuMO spectrometer a new data acquisition concept with respect to the software upgrade procedure has been developed. The fast task exchange option in the software has been implemented together with the scheme of the SAS software update for experimental data treatment. This software modification is a result of tight and successful collaboration with groups of A.Kirilov (SC Dpt., FLNP) and A.Soloviev (LIT), which has made it possible to prevent losses in the experimental time. The autonomous vacuum system for pumping out large (> 20 m^3) air volume from the vacuum tube of the detecting system has been implemented, which ensures reliable operation of the instrument and prompt corrections of problems during the opening/closing of the vacuum valves in both methodological experiments and experiments in the framework of the spectrometer modernization program.

On the neutron radiography and tomography spectrometer simulation energy-selective radiography experiments have been conducted [17]. In the experiments a CCD-camera-based detector was used. The frequency of the camera was synchronized with the reactor pulse frequency. Using the camera response delay relative to the start of reactor pulses and the exposure time variation, neutron images of various metal materials (aluminum, steel, lead, copper) have been obtained in the neutron wavelength ranges of 0.2-2, 2-3.7, 3.8-8 Å (**Fig. 26**).
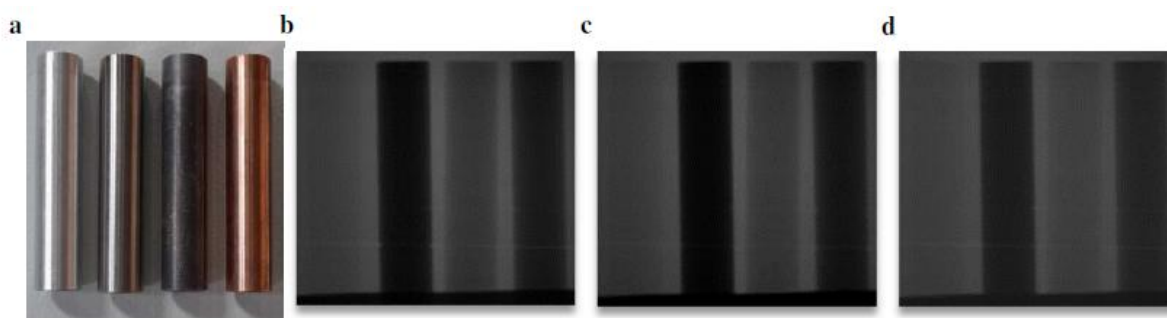

Fig. 26. Photo of cylindrical samples (aluminum, steel, lead, copper) (a) and their neutron images obtained in the wavelength ranges of 0.2-2 Å (b), 2-3.7 Å (c), 3.8-8 Å (d).

A change was observed in the contrast of images of the materials in the ranges under study, which offers good prospects for further development of energy-selective radiography and tomography at the IBR-2 reactor.

References

[1]   D.P.Kozlenko, N.T.Dang, S.E.Kichanov, E.V.Lukin, A.M.Pashayev, S.G.Jabarov, L.S.Dubrovinsky, H.-P.Liermann, W.Morgenroth, A.I.Mammadov, R.Z.Mekhtieva, V.G.Smotrakov, and B.N.Savenko "Competing magnetic states in multiferroic YMn$_2$O$_5$ at high pressure", Physical Review B, v. 92, p. 134409 (1-7) (2015).

[2]   N.V.Kosova, I.A.Bobrikov, O.A.Podgornova, A.M.Balagurov, A.K.Gutakovskii Perculiarities of structure, morphology, and electrochemistry of the doped 5-V spinel cathode materials LiNi$_{0.5-x}$Mn$_{1.5-y}$M$_{x+y}$O$_4$ (M=Co, Cr, Ti; x+y = 0.05) prepared by mechanochemical way. Journal of Solid State Electrochemistry (2015) DOI: 10.1007/s10008-015-3015-4.

[3]   A.I.Gusev, A.S.Kurlov, I.A.Bobrikov, A.M.Balagurov "V$_8$C$_{7-\delta}$ Superstructure in Nonstoichiometric Vanadium Carbide Powders" JETP Letters, 2015, Vol. 102, No. 3, pp. 154–160.

[4]   A.I.Gusev, A.S.Kurlov, E.Y.Gerasimov, A.M.Balagurov, I.A.Bobrikov, A.A.Rempel "Nanocrystalline ordered vanadium carbide: Superlattice and nanostructure", Superlattices and Microstructures (2015) submitted.

[5]   A.V.Trukhanov, V.O.Turchenko, I.A.Bobrikov, S.V.Trukhanov, I.S.Kazakevich, A.M.Balagurov "Crystal structure and magnetic properties of the $BaFe_{12-x}Al_xO_{19}$ (x = 0.1–1.2) solid solutions", J. Magn. Magn. Mater., v.393, pp.253-259 (2015).

[6]   N.M.Belozerova, S.E.Kichanov, Z.Jírak, D.P.Kozlenko, M.Kačenka, O.Kaman, E.V.Lukin, B.N.Savenko "High pressure effects on the crystal and magnetic structure of nanostructured manganites $La_{0.63}Sr_{0.37}MnO_3$ and $La_{0.72}Sr_{0.28}MnO_3$", Journal of Alloys and Compounds, v. 646, pp. 998-1003 (2015).

[7]   M.V.Avdeev, V.I.Petrenko, I.V.Gapon, L.A.Bulavin, A.A.Vorobiev, O.Soltwedel, M.Balasoiu, L.Vekas, V.Zavisova, P.Kopcansky "Comparative structure analysis of magnetic fluids at interface with silicon by neutron reflectometry", Appl. Surf. Sci., v. 352, pp. 49–53 (2015).

[8]   M.Rajnak, V.I.Petrenko, M.V.Avdeev, O.I.Ivankov, A.Feoktystov, B.Dolnik, J.Kurimsky, P.Kopcansky, M.Timko "Direct observation of electric field induced pattern formation and particle aggregation in ferrofluids", Applied Physics Letters, v. 107, p. 073108 (2015).

[9]   R.A.Eremin, Kh.T.Kholmurodov, V.I.Petrenko, L.Rosta, N.A.Grigoryeva, M.V.Avdeev On the microstructure of organic solutions of mono-carboxylic acids: Combined study by infrared spectroscopy, small-angle neutron scattering and molecular dynamics simulations. Chemical Physics v. 461, pp. 1-10 (2015).

[10]   O.V.Tomchuk, D.S.Volkov, L.A.Bulavin, A.V.Rogachev, M.A.Proskurnin, M.V.Korobov, M.V.Avdeev "Structural characteristics of aqueous dispersions of detonation nanodiamond and their aggregate fractions by small-angle neutron scattering", Journal of Physical Chemistry C, v. 119, pp. 794-802 (2015).

[11]   Yu.I.Prylutskyy, V.V.Cherepanov, M.P.Evstigneev, O.A.Kyzyma, V.I.Petrenko, V.I.Styopkin, L.A.Bulavin, N.A.Davidenko, D.Wyrzykowski, A.Woziwodzka, J.Piosik, R.Kaźmierkiewicz, U.Ritter "Structural self-organization of C60 and cisplatin in physiological solution", Phys.Chem.Chem.Phys., 2015, V. 17, P. 26084-26092.

[12]   Yu.I.Prylutskyy, M.P.Evstigneev, V.V.Cherepanov, O.A.Kyzyma, L.A.Bulavin, N.A.Davidenko, P.Scharff "Structural organization of C60 fullerene, doxorubicin, and their complex in physiological solution as promising antitumor agents", J. Nanopart. Res., 2015, 17:45.

[13]   N.Jargalan, T.V.Tropin, M.V.Avdeev, V.L.Aksenov "Investigation and modeling of evolution of UV-Vis spectra of C60/NMP solution", Nanosystems: physics, chemistry, mathematics, 2015, accepted.

[14]   T.B.Feldman, A.I.Ivankov, T.N.Murugova, A.I.Kuklin, P.V.Shelyakin, M.A.Yakovleva, V.I.Gordeliy, A.V.Belushkin, M.A.Ostrovsky "Study of visual pigment rhodopsin supramolecular organization in photoreceptor membrane by small-angle neutron scattering method with contrast variation", Proceedings of the Russian Academy of Sciences, v. 465, № 5, pp. 1-5, 2015 (in Russian).

[15]   K.Łuczyńska, K.Drużbicki, K.Łyczko, J.Cz.Dobrowolski "Experimental (X-ray, 13C CP/MAS NMR, IR, RS, INS, THz) and Solid-State DFT Study on (1:1) Co-Crystal of Bromanilic Acid and 2,6- Dimethylpyrazine", Journal of Physical Chemistry B, v. 119, p. 6852-6872 (2015).

[16]   D.M.Itkis, J.J.Velasco-Velez, A.Knop-Gericke, A.Vyalikh, M.V.Avdeev, L.V.Yashina "Probing of electrochemical interfaces by photons and neutrons in operando", ChemElectroChem, v. 2, p. 1427–1445 (2015).

[17]   E.V.Lukin, D.P.Kozlenko, S.E.Kichanov, A.V.Rutkauskas, G.D.Bokuchava, B.N.Savenko "First attempts on energy-selective neutron imaging at IBR-2", Physics Procedia, v. 69 (2015), p. 271 – 274.